

## Article

# Characterization, Kinetic Using Deconvolution Techniques and Thermodynamic Study of Synthetic $\text{MgHPO}_4 \cdot 3\text{H}_2\text{O}$

Saifon Kullyakool<sup>1,2</sup>, Somphob Thompho<sup>3</sup>, Banjong Boonchom<sup>1,2,\*</sup>  and Pesak Rungrojchaipon<sup>1</sup>

<sup>1</sup> Material Science for Environmental Sustainability Research Unit, Department of Chemistry, School of Science, King Mongkut's Institute of Technology Ladkrabang, Bangkok 10520, Thailand

<sup>2</sup> Municipal Waste and Wastewater Management Learning Center, School of Science, King Mongkut's Institute of Technology Ladkrabang, Bangkok 10520, Thailand

<sup>3</sup> Pharmaceutical Research Instrument Center, Faculty of Pharmaceutical Sciences, Chulalongkorn University, Pathumwan, Bangkok 10330, Thailand

\* Correspondence: kbbanjon@gmail.com or banjon.bo@kmitl.ac.th; Tel.: +66-2329-8400 (ext. 8411); Fax: +66-2329-8412

**Abstract:**  $\text{MgHPO}_4 \cdot 3\text{H}_2\text{O}$  was synthesized via a simple wet reaction and transformed to its final decomposed product,  $\text{Mg}_2\text{P}_2\text{O}_7$  at 873 K. The thermal properties, vibrational modes of block units, and solid phases of the synthetic compounds have been investigated by TG/DTG/DTA, FTIR, and XRD techniques. The temperature dependence of thermodynamic properties estimated from the DSC data occurred in two regions (before and after the dehydration reaction) indicating a characteristic of the prepared  $\text{MgHPO}_4 \cdot 3\text{H}_2\text{O}$  sample. The dehydration reactions of 3.5 mol of water molecules in the structure overlapped in the temperature of 363–823 K and showed the phase transition at 921 K as revealed by TG/DTG/DTA. The deconvolution technique using the newly modified co-mathematical functions was used to separate the overlapped dehydration steps in the DTG curve, which obtained the three steps. Only the first and second steps were estimated using kinetic triplet parameters ( $E_a$ ,  $A$ , and model), which indicate the single dehydration mechanism with the  $A_{1.25}$  model and the multi-step of a parallel mechanism with the  $A_{1.6}$  model, respectively. The data of kinetics and thermodynamics play key points in theoretical study, application development, and industrial production of magnesium phosphates as a theoretical basis.



**Citation:** Kullyakool, S.; Thompho, S.; Boonchom, B.; Rungrojchaipon, P. Characterization, Kinetic Using Deconvolution Techniques and Thermodynamic Study of Synthetic  $\text{MgHPO}_4 \cdot 3\text{H}_2\text{O}$ . *Crystals* **2023**, *13*, 567. <https://doi.org/10.3390/cryst13040567>

Academic Editor: Yael Diskin-Posner

Received: 2 March 2023

Revised: 19 March 2023

Accepted: 22 March 2023

Published: 27 March 2023



**Copyright:** © 2023 by the authors. Licensee MDPI, Basel, Switzerland. This article is an open access article distributed under the terms and conditions of the Creative Commons Attribution (CC BY) license (<https://creativecommons.org/licenses/by/4.0/>).

**Keywords:** co-mathematical functions deconvolution; modified master plots method; nonlinear curve fitting; temperature dependence; thermodynamic functions; complicated dehydration compound;  $\text{MgHPO}_4 \cdot 3\text{H}_2\text{O}$ ;  $\text{Mg}_2\text{P}_2\text{O}_7$

## 1. Introduction

The magnesium phosphate compounds are always stable in various hydrated forms such as struvite ( $\text{MgNH}_4\text{PO}_4 \cdot 6\text{H}_2\text{O}$ ) [1], newberyite ( $\text{MgHPO}_4 \cdot 3\text{H}_2\text{O}$ ) [2], bobierite ( $\text{Mg}_3(\text{PO}_4)_2 \cdot 8\text{H}_2\text{O}$ ) [3], and hannayite ( $\text{Mg}_3(\text{NH}_4)_2\text{H}_4(\text{PO}_4)_4 \cdot 8\text{H}_2\text{O}$ ) [4] and they can be obtained from mineral resources or produced by humans [5]. Under the heat treatment, these magnesium phosphate hydrates can change into magnesium phosphate anhydrous compounds ( $\text{Mg}_3(\text{PO}_4)_2$ ), magnesium cyclophosphate ( $\text{Mg}_2\text{P}_4\text{O}_{12}$ ), and magnesium pyrophosphate ( $\text{Mg}_2\text{P}_2\text{O}_7$ ) [6–11]. The magnesium phosphate anhydrous compounds are attractively used as heterogeneous catalysts for many organic syntheses [12–14], anti-corrosive ceramic pigments [15], and as fillers for bioactive materials [16] because they are temperature-resistant, structurally and chemically stable, and insoluble in water [17]. Aramendía et al. reported that the mix-phase of  $\text{Mg}_3(\text{PO}_4)_2$  and  $\text{Mg}_2\text{P}_2\text{O}_7$  consisting of acidic and basic site plays a role as a catalyst in the dehydration-dehydrogenation reaction of 2-hexane [13]. In 1999, the catalytic activity of  $\text{Mg}_2\text{P}_2\text{O}_7$ ,  $\text{Mg}_3(\text{PO}_4)_2$ , and  $\text{NaMg}_4(\text{PO}_4)_3$  in the gas-phase conversion of 2-hexanol was reported by Aramendía et al. [18]. Sadiq et al.

reported the catalytic activity of pure  $\text{Mg}_3(\text{PO}_4)_2$  and  $\text{Mg}_3(\text{PO}_4)_2$  modified by Co-Mo, in 3,3-dimethylbut-1-ene isomerization reaction as a gas/solid interface reaction [19]. The results showed that  $\text{Mg}_3(\text{PO}_4)_2$  has high catalytic activity in skeleton isomerization due to strong acid sites of Lewis and Brønsted acid centers [19]. In 2015, Sadiq et al. studied the catalytic activity of  $\text{Mg}_3(\text{PO}_4)_2$  and  $\text{Mg}_2\text{P}_2\text{O}_7$  in the skeletal isomerization of 3,3-dimethylbut-1-ene and the result exhibits the  $\text{Mg}_2\text{P}_2\text{O}_7$  catalyst, which has high number of active acid sites and is more active than  $\text{Mg}_3(\text{PO}_4)_2$  catalyst [14]. Moreover,  $\text{Mg}_2\text{P}_2\text{O}_7$  is an alternative non-toxic and color stable ceramic over high temperature [15]. Newberyite, a constituent of human and animal calculi, has been used as additive in bioactive material [5]. Sugiyama et al. reported the use of  $\text{MgHPO}_4$  to remove aqueous ammonium from wastewater [20]. Mohammad et al. prepared  $\text{MgHPO}_4$  bound by ethyl cellulose that can be used in the sensory, pharmaceutical, and biomedical sectors [21]. Based on the above-mentioned reports, newberyite and  $\text{Mg}_2\text{P}_2\text{O}_7$  are particularly interesting and are the joint focus of this study.

Newberyite belongs to the orthorhombic space group  $Pbca$  with eight molecules in a unit cell [2,7]. The  $\text{MgHPO}_4 \cdot 3\text{H}_2\text{O}$  structure has a strong hydrogen bond of the pair of  $\text{HPO}_4^{2-}$  molecules resulting in the complex vibrational bands of  $\text{PO}_4^{3-}$  ground [2,7]. Its final decomposition product,  $\text{Mg}_2\text{P}_2\text{O}_7$ , belongs to the monoclinic system in  $P2_1/n$  space group [2,7]. Aramendía et al. have synthesized magnesium phosphate by varying the reactant sources (Mg and P) and mole ratios of Mg to P [13]. The study found that the different sources and the ratios of Mg to P resulted in different stoichiometric compounds. Mesíková et al. synthesized  $\text{MgHPO}_4 \cdot 3\text{H}_2\text{O}$  in an ice bath from a suspension of magnesium hydroxide and a solution of phosphoric acid within a short period time (1 h) [2]. The pH effect on the synthesized product was studied and the results showed that when increasing the pH value, the growth of particle size distribution also increased, while the specific surface area decreased [2]. Boonchom studied the decomposition kinetics of the commercial  $\text{MgHPO}_4 \cdot 3\text{H}_2\text{O}$  and found that the decomposition occurred in one step as a single dehydration process with  $F_{1/3}$  model controlling mechanism [7]. Based on previous study results, the different synthetic routes for obtaining one material showed that differences in thermal behavior and other properties [16,17] might be affected to apply in a specific field, e.g., catalytic.

In this work,  $\text{MgHPO}_4 \cdot 3\text{H}_2\text{O}$  was synthesized using a simple wet chemical reaction at ambient temperature. The thermal decomposition from  $\text{MgHPO}_4 \cdot 3\text{H}_2\text{O}$  into  $\text{Mg}_2\text{P}_2\text{O}_7$  was analyzed. The deconvolution technique using co-mathematical functions was used to separate the covering decomposition step. The activation energy and pre-exponential factor were determined using the modified iterative from Kissinger, Akahira and Sonose (KAS) equations [22,23]. The mechanism function of the decomposition was confirmed by three methods; (1) the roughly observed  $g(\alpha)$  by plotting of  $d\alpha/dT$  versus  $\alpha$  and the  $g(\alpha)$  was identified by curve shape, (2) the exhaustive  $g(\alpha)$  was evaluated using the modified master plots combined with the non-linear curve fitting, (3) checking of the correction of the  $g(\alpha)$  evaluated from (2) by using the basic master plotting equation [24,25]. Additionally, the temperature dependence of the standard thermodynamic functions (the change in entropy, enthalpy, and Gibbs free energy) was evaluated from DSC results using the cubic polynomial curve fitting [26,27]. Studies on the thermodynamics, mechanisms and kinetics of thermally-decomposed reactions are challenging, with sophistication affecting the large diversity of factors, with diverse effects such as the rebuilding of solid state crystal lattices, setting-up and growth of new crystallization nuclei, diffusion of gaseous agents or reaction products, materials heat conductance, the static or dynamic feature of the environment, the physical state of the reagents, that is, dispersity, layer thickness, specific surface area and porosity, the kind, quantity, and distribution of the active centers on solid state surface, etc. [28–32]. The results obtained from such studies can be straightforward and practical in materials science for both academics and industrialists who are interested in the preparation of various metals and alloys, cement, ceramics, glasses, enamels, glazes, catalysts, and polymer and composite materials [31,33]. The key factor in obtaining  $\text{MgHPO}_4 \cdot 3\text{H}_2\text{O}$  and

Mg<sub>2</sub>P<sub>2</sub>O<sub>7</sub> with different properties has been used in different preparative methods, which could play a large role in industrial applications [31,32].

## 2. Materials and Methods

### 2.1. Synthesis and Characterization

MgHPO<sub>4</sub>·3H<sub>2</sub>O powder was synthesized by a simple wet chemical reaction. A MgCl<sub>2</sub>·6H<sub>2</sub>O solid sample was dissolved in 85% *w/w* H<sub>3</sub>PO<sub>4</sub> in the ratio of Mg:P at 1:1 and then controlled at 313 K for 2 h. After that, the resulting solution was adjusted to pH 6 by 1.0 M NaOH, and a precipitate then appeared. The white powder was isolated by filtration, then washed with deionized water and dried in open air. The synthesized hydrate was calcined at 500 and 973 K. The synthesized hydrate and the thermal treatment products were characterized using Fourier-transform infrared spectroscopy (FTIR, Perkin Elmer Spectrum GX; UK) in the wavenumber range of 4000–370 cm<sup>−1</sup> by KBr pellet technique (spectroscopy grade of KBr, Merck; Germany), thermogravimetry, derivative thermogravimetry, and differential thermal analysis (TG/DTG/DTA, Perkin Elmer Pyris Diamond; Waltham, MA, USA), and X-ray powder diffraction (XRD, Phillips 3710; UK) technique with CuK<sub>α</sub> radiation (λ = 1.5406 nm) over the 2θ range of 5° < 2θ < 70°.

### 2.2. The Temperature Dependence of the Thermodynamic Functions

Heat capacity (C<sub>p</sub>) of MgHPO<sub>4</sub>·3H<sub>2</sub>O and Mg<sub>2</sub>P<sub>2</sub>O<sub>4</sub> were determined using DSC (Perkin-Elmer Pyris1) technique measuring within the temperature range from 323 to 823 K at heating rate of 10 K min<sup>−1</sup> under N<sub>2</sub> atmosphere with sample mass of 4.5 mg (accurate). The isobaric molar heat capacity, C<sub>p</sub>(T), derived from the ratio of the actual DSC heat flow (ΔP/mW) and applied heating rate (β/K min<sup>−1</sup>) is expressed as the equation [34].

$$C_p(T) = \frac{1}{m} \left( \frac{dH}{dT} \right) = \frac{1}{m} \left( \frac{dH/dt}{dT/dt} \right) = \frac{1}{m} \left( \frac{\Delta P}{\beta} \right)$$

where, m is the sample mass (g). The temperature dependence of C<sub>p</sub>(T) can be evaluated from non-linear regression using cubic polynomial curve fitting. Moreover, the temperature dependence of standard thermodynamic functions such as entropy, enthalpy and Gibbs free energy can be estimated from C<sub>p</sub>(T) with the following Equations (1)–(3) [16].

$$\Delta S^\circ = S_T^\circ - S_{298.15}^\circ = \int_{298.15}^T \left( \frac{C_p(T)}{T} \right) dT + \frac{\Delta H_t}{T_t} + \int_{T_t}^{T_m} \left( \frac{C_p(T)}{T} \right) dT + \frac{\Delta H_m}{T_m} + \int_{T_m}^{T_T} \left( \frac{C_p(T)}{T} \right) dT \quad (1)$$

$$\Delta H^\circ = H_T^\circ - H_{298.15}^\circ = \int_{298.15}^{T_t} C_p(T) dT + \Delta H_t + \int_{T_t}^{T_m} C_p(T) dT + \Delta H_m + \int_{T_m}^{T_T} C_p(T) dT \quad (2)$$

$$\Delta G^\circ = G_T^\circ - G_{298.15}^\circ = \left( H_T^\circ - H_{298.15}^\circ \right) - T \left( S_T^\circ - S_{298.15}^\circ \right) \quad (3)$$

### 2.3. Kinetic Study of Thermal Transformation

The kinetic study of MgHPO<sub>4</sub>·H<sub>2</sub>O was carried out by TG/DTG/DTA at four heating rates (10, 15, 20, and 25 K min<sup>−1</sup>) over the temperature range of 303–1073 K. The mathematical deconvolution method was used to separate the covered DTG peaks and then the kinetic parameters in each step were determined [25].

Mathematical Deconvolution. The mathematical deconvolution technique as a popular technique was used to separate the covering peaks [24,25]. The numerous mathematical functions were used to separate the unclearly divided peaks as shown below.

1. Gaussian Function: Ref. [25] There Are Many Versions of Gaussian Functions:

Normal Gaussian peak function

$$y = \frac{1}{\sigma\sqrt{2\pi}} \exp \left[ -\frac{(x - x_c)^2}{2\sigma^2} \right] \quad (4)$$

Amplitude version of Gaussian peak function

$$y = A \exp \left[ -\frac{(x - x_c)^2}{2\sigma^2} \right] \tag{5}$$

$$A = \frac{a}{2\sigma\sqrt{\frac{\pi}{2}}} \tag{6}$$

Bi-Gaussian peak function

$$y = H \exp \left[ -\frac{(x - x_c)^2}{2\sigma_1^2} \right], (x < x_c) \tag{7}$$

$$y = H \exp \left[ -\frac{(x - x_c)^2}{2\sigma_2^2} \right], (x \geq x_c) \tag{8}$$

$$H = \frac{a}{\sigma\sqrt{2\pi}} \tag{9}$$

Constrained Gaussian peak function

$$y = \frac{A}{(\sigma_1 + \sigma_2 x_c)\sqrt{2\pi}} \exp \left[ -\frac{(x - x_c)^2}{2(\sigma_1 + \sigma_2)^2} \right] \tag{10}$$

2. Amplitude Version of Weibull Peak Function

$$y = A \frac{(\sigma_2 - 1)^{\left(\frac{1-\sigma_2}{\sigma_2}\right)}}{\sigma_2} (S)^{(\sigma_2-1)} \exp \left[ -S^{\sigma_2} + \left(\frac{\sigma_2 - 1}{\sigma_2}\right) \right] \tag{11}$$

$$S = \frac{x - x_c}{\sigma_1} + \left(\frac{\sigma_2 - 1}{\sigma_2}\right)^{1/\sigma_2} \tag{12}$$

$$A = \frac{a}{\sigma_1\sigma_2\sqrt{\frac{\pi}{2}}} \tag{13}$$

3. Fraser-Suzuki Peak Function

$$y = H \exp \left\{ -\frac{\ln 2}{S} \ln \left[ 1 + 2S \frac{(x - x_c)^2}{2\sigma^2} \right] \right\} \tag{14}$$

where the peak parameters such as  $\sigma$ ,  $A$ ,  $H$ ,  $x_c$ , and  $S$  are standard deviation, amplitude, peak high, center, and asymmetric parameters (dimensionless), respectively.

The Gaussian and Fraser-Suzuki functions are the most popular ones to use to separate the covering peak [24,25,35]. In this work, the co-mathematical functions combining the deconvolution technique were performed. Equations (4)–(14) were tested to separate the covering DTG curve and the suitable functions were selected by minimizing the residual sum of square (RSS) and  $R^2$  close to 1.000.

Kinetic parameters determination. The activation energy ( $E$ ) and pre-exponential factor ( $A$ ) were determined after deconvolution treatment. The  $E$  and  $A$  values were evaluated using the iterative modified KAS method as the following equation [22,23].

$$\ln \left( \frac{\beta}{T^2} \right) = \ln \left( \frac{AR}{g(\alpha)E} \right) - \frac{E}{RT} \tag{15}$$

Equation (15) was modified to be

$$\ln\left(\frac{\beta}{h(x)T^2}\right) = \ln\left(\frac{AR}{g(\alpha)E}\right) - \frac{E}{RT} \quad (16)$$

where  $x = E/RT$  and  $h(x)$  is expressed by the 4th-order of Senum-Yang approximation formula as following the equation [36].

$$h(x) = \frac{x^4 + 18x^3 + 86x^2 + 96x}{x^4 + 20x^3 + 120x^2 + 240x + 120} \quad (17)$$

The iterative procedure can be performed by following steps:

- (i) Assume  $h(x) = 1$  to estimate the initial value of  $E_1$ . The isoconversional methods stop the calculation at this step.
- (ii) Using  $E_1$ , calculate a new value of  $E_2$  from the plot of  $\ln[\beta/h(x)T^2]$  versus  $1000/T$ .
- (iii) Repeat step (ii), replacing  $E_1$  with  $E_2$ . When  $E_i - E_{i-1} < 0.1 \text{ kJ mol}^{-1}$ , the last value of  $E_i$  was considered to be the exact value of the activation energy of the reaction.

The pre-exponential factor  $A$  was calculated using Equation (15) by substituted  $g(\alpha)$ .

Moreover, the Kissinger equation was used to calculate the kinetic parameters,  $E$  and  $A$  of the fourth step.

$$\ln\left(\frac{\beta}{T_p^2}\right) = \ln\left(\frac{AR}{E}\right) - \frac{E}{RT_p} \quad (18)$$

According to Equation (18), plotting of  $\ln(\beta/T_p^2)$  versus  $1000/T_p$  in four heating rates then the  $E$  and  $A$  can be calculated from slope and y-intercept, respectively.

Mechanism function determination. The mechanism function of the dehydration step in this work was determined using the non-linear method accepted from ICTAC Kinetics Committee recommendations in 2011 appropriating for evaluation of the kinetic parameters whether that of single-step or multi-step reaction [37,38].

From the rate equation

$$\frac{d\alpha}{dT} = \frac{A}{\beta} e^{-E_\alpha/RT} f(\alpha) \quad (19)$$

where  $f(\alpha)$  is the differential form of the mechanism function. Integrating Equation (19) yields the integral form of the mechanism function  $g(\alpha)$  as following the equation:

$$g(\alpha) = \int_0^\alpha \frac{1}{f(\alpha)} d\alpha = \frac{AE_\alpha}{\beta R} p(x) \quad (20)$$

where,

$$p(x) = \int_x^\infty \frac{e^x}{x^2} dx \quad (21)$$

$$p(x) = \frac{e^{-x}}{x^2} h(x) \quad (22)$$

From Equation (19), referring to  $\alpha = 0.5$ , the master plots equation is obtained as follows:

$$\frac{g(\alpha)}{g(0.5)} = \frac{p(x)}{p(x_{0.5})} \quad (23)$$

$$(Y)_{exp} = \frac{p(x)}{p(x_{0.5})} \quad (24)$$

$$(Y)_{Theory} = \frac{g(\alpha)}{g(0.5)} \quad (25)$$

The theoretical plots of  $g(x)/g(0.5)$  can be obtained for the different kinetic mechanism functions at the reported 35 functions [24,25,35]. Based on Equation (24), the plots of  $p(x)/p(x_{0.5})$  versus  $\alpha$  are the experimental plots [39]. In this work, the modified master plots combined with the non-linear curve fitting method are used to evaluate the correct  $g(\alpha)$  and the general equation as following the equations:

$$\text{F models : } g(\alpha) = \frac{1}{n-1}(1-\alpha)^{1-n} - 1 \quad (26)$$

$$\text{R models : } g(\alpha) = 1 - (1-\alpha)^{1/n} \quad (27)$$

$$\text{P models : } g(\alpha) = \alpha^{1/n} \quad (28)$$

$$\text{A models : } g(\alpha) = [-\ln(1-\alpha)]^{1/n} \quad (29)$$

From the Equations (8) and (10)–(12), the nonlinear master plots curve fitting equations can be expressed following the equations.

$$\text{F models : } \frac{g(\alpha)}{g(0.5)} = \frac{(1-\alpha)^{(1-n)} - 1}{0.5^{(1-n)} - 1} \quad (30)$$

$$\text{R model : } \frac{g(\alpha)}{g(0.5)} = \frac{1 - (1-\alpha)^{1/n}}{1 - 0.5^{1/n}} \quad (31)$$

$$\text{P models : } \frac{g(\alpha)}{g(0.5)} = \frac{\alpha^{1/n}}{0.5^{1/n}} \quad (32)$$

$$\text{A models : } \frac{g(\alpha)}{g(0.5)} = \frac{[-\ln(1-\alpha)]^{1/n}}{[-\ln 0.5]^{1/n}} \quad (33)$$

Equations (29)–(32) are tested by the fitting of the  $n$ -order according to 35 (Table S1) reported functions and the results show that the  $R^2$  is equal to 1.000. The mechanism functions evaluated from the modified master plots combined with the non-linear curve fitting method were double-checked using Equation (20) by comparing the  $g(\alpha)$  from the experimental and that of theoretical (Table S1) by minimization of the residual sum of square (RSS) [25,38].

$$RSS = \sum [g(\alpha)_{exp} - g(\alpha)_{Theo}]^2 \quad (34)$$

### 3. Results and Discussion

#### 3.1. Characterization

The synthesized hydrate and the calcined products at 723 and 923 K (4 h in air atmosphere) were characterized by TG/DTG/DTA, FTIR, XRD, and DSC techniques.

TG/DTG/DTA results. The TG/DTG/DTA curves are shown in Figure 1. The loss weight exhibited in the TG curve in the range of 363–823 K was found to be 35.79%, which is equal to 3 molecules of water of crystallization and 0.5 molecules of water of constituent. The corresponding peak observed at 435 K in DTG and DTA curves was related to the endothermic reaction. This confirms that the dehydration reactions of 3.5 molecules of water in the structure have overlapped. Moreover, there was an exothermic DTA peak at 921 K attributing that to be due to the phase transition from lower to higher crystallinities as confirmed by the FTIR (Figure 2) and XRD (Figure 3) results, and the thermal transformation reaction of  $\text{MgHPO}_4 \cdot 3\text{H}_2\text{O}$  is shown in the Equation (35). The thermal behavior of the synthesized  $\text{MgHPO}_4 \cdot 3\text{H}_2\text{O}$  compound in this work differed from that of the commercial  $\text{MgHPO}_4 \cdot 3\text{H}_2\text{O}$  compound reported in previous work [7].

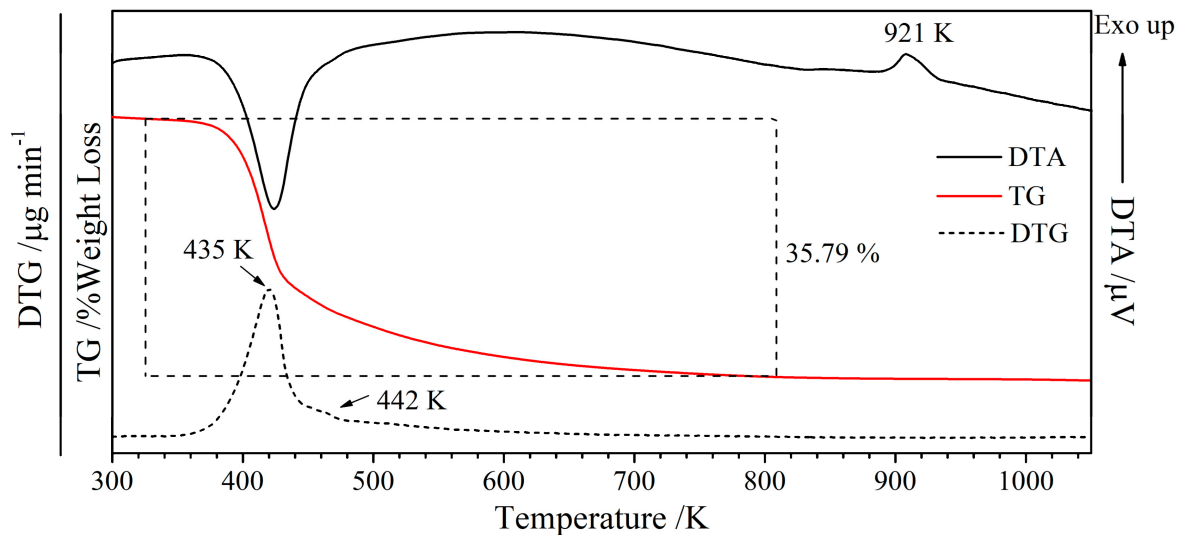
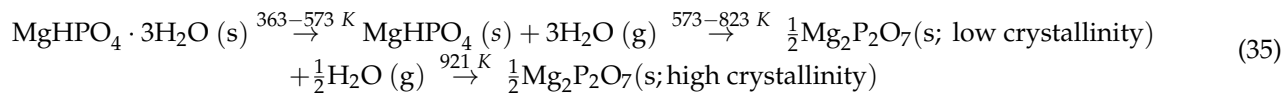


**Figure 1.** TG/DTG/DTA curves of  $\text{MgHPO}_4 \cdot 3\text{H}_2\text{O}$  at over the temperature range of 303–1073 K at a heating rate of  $10 \text{ K min}^{-1}$  under  $\text{N}_2$  atmosphere.

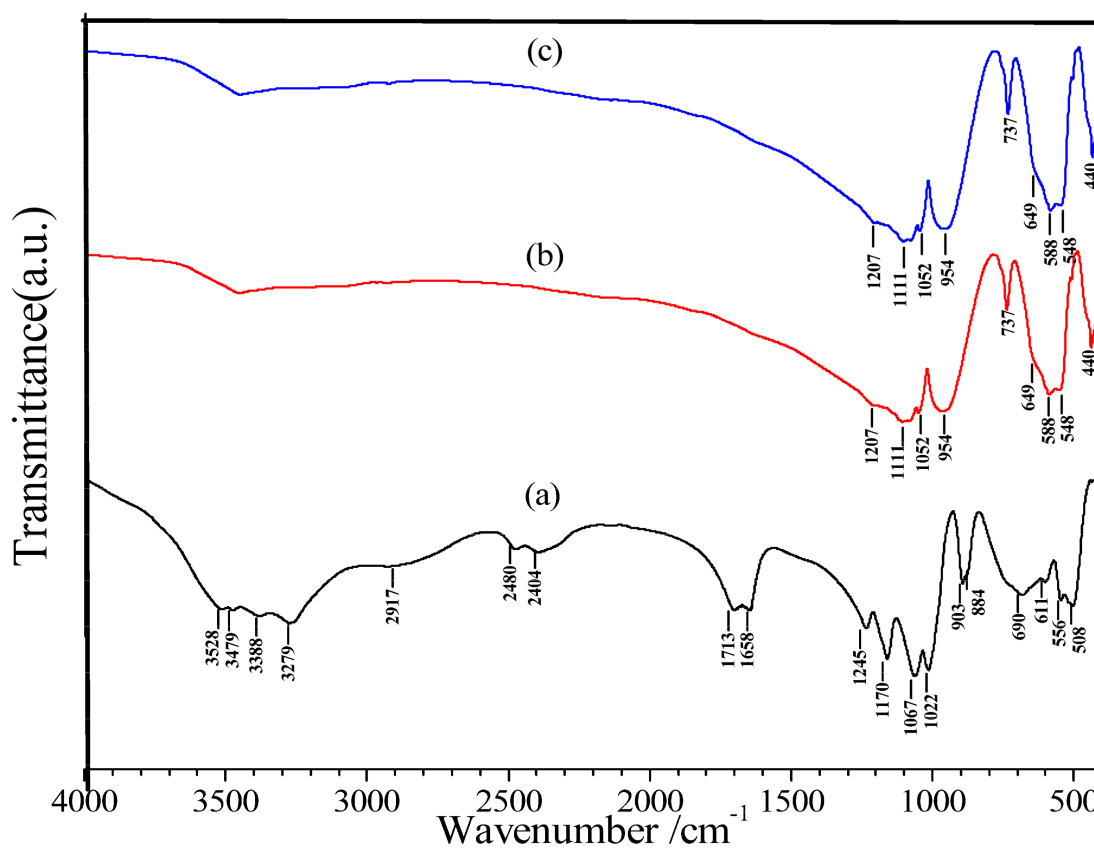


**Figure 2.** FTIR spectra: (a) the synthesized hydrate, (b) the calcined products at 773 K, and (c) the calcined products at 973 K.

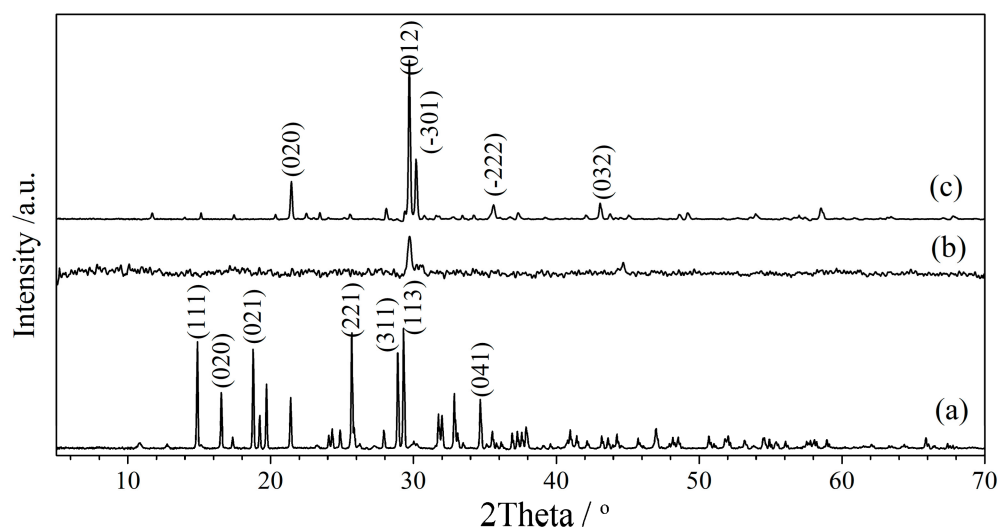


**Figure 3.** XRD patterns: (a)  $\text{MgHPO}_4 \cdot 3\text{H}_2\text{O}$ , (b) the calcined products at 773 K, and (c) the calcined products at 973 K (4 h in air atmosphere).

**FTIR result.** The FTIR spectra of the synthesized hydrate and the calcined products at 773 and 973 K are illustrated in Figure 2. The spectrum of the hydrate (Figure 2a) exhibits the vibrational bands of water at around  $3500\text{--}3200\text{ cm}^{-1}$ ,  $1700\text{--}1600\text{ cm}^{-1}$ , and  $700\text{ cm}^{-1}$ . The vibrational bands of  $\text{HPO}_4^{2-}$  are demonstrated to be the complex character such as A-B-C trio bands of the two forming components due to the stretching of the strongly H-bonded hydrogenphosphate [2,4,7]. Normally, the B band ( $2900\text{ cm}^{-1}$ ) is stronger than A and C bands ( $2400\text{ cm}^{-1}$ ), while the C band is covered up by the vibrational (banding) band of water appearing at around  $1600\text{ cm}^{-1}$ . In the case of the calcined products at 773 and 973 K (Figure 2b,c), the spectra are quite similar, which do not appear in the vibrational bands of water and exhibit the vibration frequencies at low regions indicating the character of  $[\text{P}_2\text{O}_7]^{4-}$  anion. The fundamental vibrational modes of  $[\text{P}_2\text{O}_7]^{4-}$  anion containing the P-O stretching, symmetric  $\text{PO}_2$  stretching ( $\nu_{\text{sym}}, \text{PO}_2$ ), asymmetric  $\text{PO}_2$  stretching ( $\nu_{\text{asym}}, \text{PO}_2$ ), symmetric ( $\nu_{\text{sym}}, \text{POP}$ ), asymmetric stretch ( $\nu_{\text{asym}}, \text{POP}$ ) bridge, and  $\text{PO}_3$  deformation and rocking modes, the POP deformations and the torsional and external modes are known to appear in the ranges of  $1150\text{--}960$ ,  $954$ ,  $1082$ ,  $649$ ,  $737$ ,  $580\text{--}420\text{ cm}^{-1}$ , respectively [15,18].

**XRD result.** The XRD patterns of the hydrate, the calcined product at 773 and 973 K (4 h in air atmosphere) are shown in Figure 3 and the results show that the hydrate and the calcined products (773 and 973 K) are  $\text{MgHPO}_4 \cdot 3\text{H}_2\text{O}$  and  $\text{Mg}_2\text{P}_2\text{O}_7$ , respectively. The XRD pattern of the calcined product at 773 K observed low intense peaks points to the character of amorphous phase or low crystallinity of  $\text{Mg}_2\text{P}_2\text{O}_7$ . The pattern of the hydrate (Figure 3a) agrees with the standard PDF #72-0023 ( $\text{MgHPO}_4 \cdot 3\text{H}_2\text{O}$ ) crystallizing in the orthorhombic system with space group  $Pbca$ . The patterns of calcined product at 973 K (Figure 3c) agrees with the PDF #32-0626 crystallizes in the monoclinic system with space group  $P_{21/n}$  [2,5,7,13]. These results agree well with the results from TG/DTG/DTA and FTIR. The final decomposition product,  $\text{Mg}_2\text{P}_2\text{O}_7$  completely occurs after the temperature of 921 K as an exothermic temperature attributed to being due to phase transition from lower to higher crystallinity [13].

### 3.2. The Temperature Dependence of the Thermodynamic Functions

The result from the measurement of DSC carrying out over the temperature range of  $323\text{--}823\text{ K}$  at a heating rate of  $10\text{ K min}^{-1}$  under  $\text{N}_2$  atmosphere exhibits three endothermic peaks of the transitions as shown in Figure 4. The transition temperatures on the DSC curve appearing at a higher temperature than that on TG/DTG/DTA curves may be due to the high sensitivity of DSC technique [26,27]. However, the results from DSC and TG/DTG/DTA techniques agree with each other. Figure 4a illustrates the  $C_p(T)$  curve divided into two regions consisting of; region I ( $323\text{--}383\text{ K}$ ) and region II ( $518\text{--}583\text{ K}$ ),

a region after dehydration. It can be seen that the  $C_p(T)$  equations of both regions show the fine cubic polynomial relationships with temperature from 323 to 383 and 518 to 583 K, which confirm the correlation coefficient of fitting  $R^2$  as 0.9995 and 0.998, respectively. Although the observed temperature is from 323 to 383 and 518 to 583 K, the equations of  $C_p(T)$  are stable and continuous, which can serve as a guide for the application of the studied compound in the temperature. The entropy  $\Delta S^\circ(T)$ , enthalpy  $\Delta H^\circ(T)$ , and Gibbs free energy  $\Delta G^\circ(T)$  changes from two temperature ranges (323–383 and 518–583 K) taking 298.15 as the benchmark temperature were calculated by Equations (1)–(3). The results are shown in Equations (36)–(43).

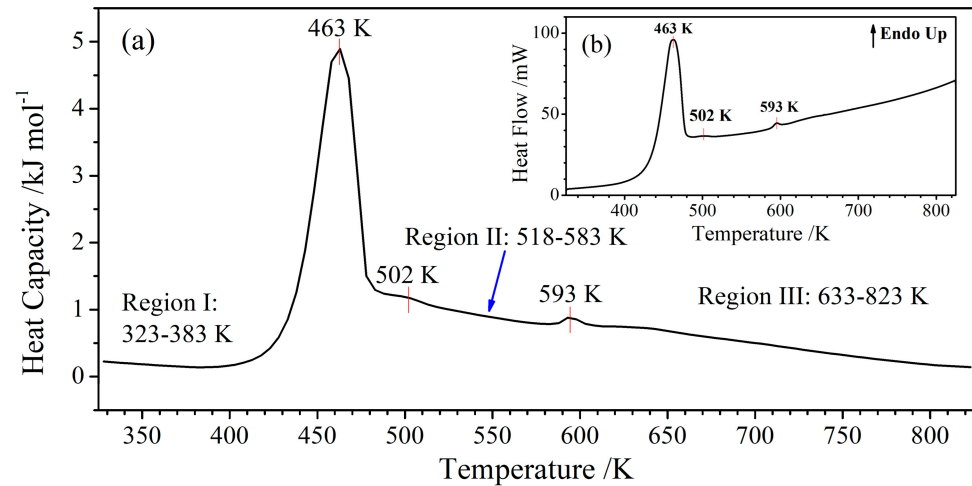


Figure 4. DSC result: (a) heat capacity curve of  $\text{MgHPO}_4 \cdot 3\text{H}_2\text{O}$  and (b) heat flow curve.

Region I;  $T_1 = 323\text{--}383\text{ K}$

$$C_p(T_1) = 133.39 - 1.28T + 4.20 \times 10^{-3}T^2 - 4.50 \times 10^{-6}T^3 \left( \text{kJ K}^{-1}\text{mol}^{-1} \right); R^2 = 0.9995 \quad (36)$$

$$\Delta S^\circ(T_1) = -519.94 + 133.39 \ln T - 1.28T + 2.10 \times 10^{-3}T^2 - 1.50 \times 10^{-6}T^3 \left( \text{kJ K}^{-1}\text{mol}^{-1} \right) \quad (37)$$

$$\Delta H^\circ(T_1) = 33270 + 133.39T - 1.14T^2 + 1.40 \times 10^{-3}T^3 - 1.12 \times 10^{-6}T^4 \left( \text{kJ mol}^{-1} \right) \quad (38)$$

$$\Delta G^\circ(T_1) = 33270 + 653.33T - 133.39T \ln T + 0.14T^2 - 7.00 \times 10^{-4}T^3 + 3.80 \times 10^{-7}T^4 \left( \text{kJ mol}^{-1} \right) \quad (39)$$

Region II;  $T_2 = 518\text{--}583\text{ K}$

$$C_p(T_2) = -72.16 + 0.3511T - 2.46 \times 10^{-4}T^2 + 2.37 \times 10^{-7}T^3 \left( \text{kJ K}^{-1}\text{mol}^{-1} \right); R^2 = 0.9998 \quad (40)$$

$$\Delta S^\circ(T_2) = 315.56 - 72.16 \ln T + 0.3511T - 1.23 \times 10^{-4}T^2 + 7.90 \times 10^{-8}T^3 \left( \text{kJ K}^{-1}\text{mol}^{-1} \right) \quad (41)$$

$$\Delta H^\circ(T_2) = 7728.85 - 72.16T + 0.1756T^2 - 8.2 \times 10^{-5}T^3 + 5.92 \times 10^{-8}T^4 \left( \text{kJ mol}^{-1} \right) \quad (42)$$

$$\Delta G^\circ(T_2) = 7728.85 - 387.72T + 72.16T \ln T - 0.1755T^2 + 4.10 \times 10^{-5}T^3 - 1.98 \times 10^{-8}T^4 \left( \text{kJ mol}^{-1} \right) \quad (43)$$

The dependence of thermodynamic properties on temperatures is shown in Equations (36)–(43), which are characteristic of the prepared  $\text{MgHPO}_4 \cdot 3\text{H}_2\text{O}$  samples, which occurred in two regions: the first (I) region is before the dehydration (hydrate being transformed) reaction and the second (II) region is after the dehydration (occurred anhydrous form) process. However, Equations (41)–(43) used for estimation will give slightly inaccurate due

to the covered peaks of the DSC curve resulting in the unrealistic  $\Delta H$  and  $T_p$  (peak temperature). When calculated in the individual temperature ranges, the values of  $\Delta S^\circ(T)$ ,  $\Delta H^\circ(T)$ , and  $\Delta G^\circ(T)$  increase with the rise in temperature. The calculated results showed that the equations of the entropy and Gibbs free energy changes exhibit logarithmic temperature dependence, while the enthalpy change has a non-linear relationship with temperature. These results can give valuable information for both theory and applications of magnesium phosphate materials, which are used to consider its phase transformation affecting the catalytic application.

### 3.3. Kinetic Study

The kinetic study of  $\text{MgHPO}_4 \cdot \text{H}_2\text{O}$  was carried out by measuring TG/DTG/DTA at four heating rates (10, 15, 20, and 25  $\text{K min}^{-1}$ ). The three steps of the dehydration reactions are not clearly separated difficult to determine the kinetic parameter. Therefore, the mathematical deconvolution method was used to separate into the DTG peaks to further determine the kinetic parameters in each step.

**Mathematical Deconvolution.** The DTG curve was separated to three steps by co-functions of the deconvolution method by using Equations (4)–(14) and the suitable functions consist of Bi-Gaussian, Amplitude version of Gaussian, and Fraser-Suzuki peak functions for the first (I), second (II), and third (III) steps, respectively [24,25,29,39]. The deconvolution of DTG curves and the  $d\alpha/dT$  vs. T curves of the I and II steps of four heating rates are shown in Figure 5 with the minimizing of RSS and  $R^2$  close to 1.000, which is a factor used to confirm the realistic of the deconvolution method. For the third step, the deconvolution method is not applied because the reason for the realistic is caused. The comparison between the simulated TG curves and the experimental TG curves of four heating rates exhibited in Figure 6 shows no significant difference.

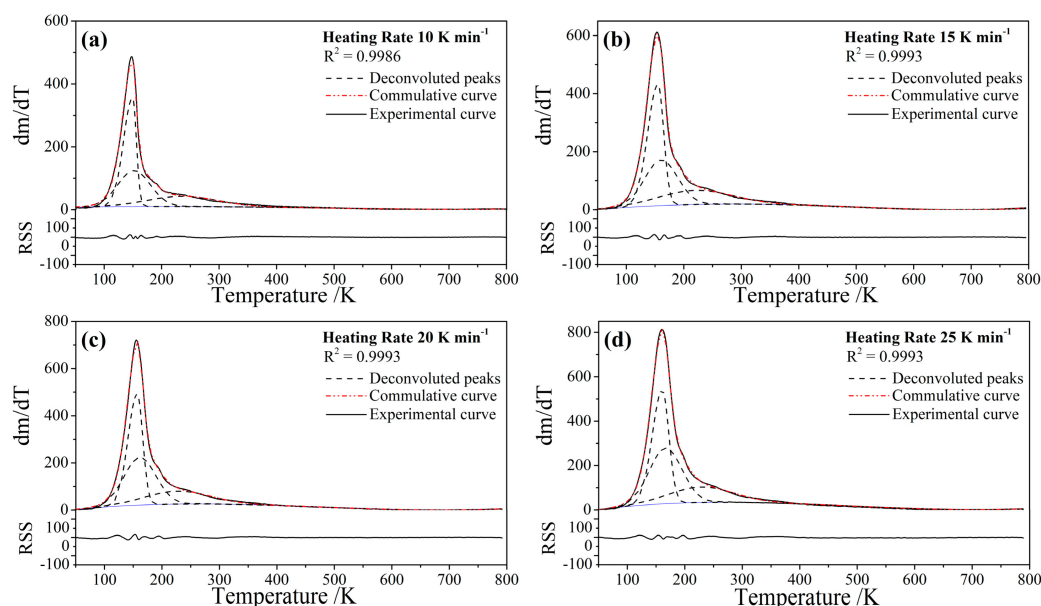


**Figure 5.** Four deconvoluted DTG peaks were observed from overlapped DTG peaks from modified co-mathematical functions for the experimentally observed DTG curve of the studied thermal solid-state reaction.

**Activation energy determination.** After the three covering steps were separated, the percentages of weight loss of each step were simulated by integrating the deconvolution treated curves (Figures 5 and 6). The modified iterative from KAS equation was used to determine the activation energy as shown in Table 1. The % relative error values of the first step, which are less than 10%, illustrate the independence of activation energies on the conversion fractions,  $\alpha$ , and confirm that the dehydration step is the single step mechanism. The second step consists of more than 10% of the relative error values contributed

to the multi-step mechanism of the decomposition presumed due to the parallel of the two mechanisms [22,23,37]. The third step shows the widely distributing activation energy values contributed that the mechanism consists of many processes such as the physical and chemical processes of the changes, therefore the realistic of the kinetic parameters are difficult to determine. This result is consistent with the deconvolution method for the third step. The average activation energies for the three steps obtained in this work are different from those of the single step reported in previous work found to be about  $100 \text{ kJ/mol}^{-1}$  calculated by Ozawa, KAS, and iterative methods [7]. The obtained  $E_a$  values of the first separated peak are higher than that for the second separated peak, which could be due to a stronger H-bond in first water molecules than that of the H-bond in second water molecules. In order to break the H-bond, the dehydration process of the starting compound ( $\text{MgHPO}_4 \cdot 3\text{H}_2\text{O}$ ) requires higher  $E_a$  values than that of the dehydration process of  $\text{MgHPO}_4 \cdot n\text{H}_2\text{O}$  ( $0 < n < 2$ ) supporting the stability of the hydrate formula form.

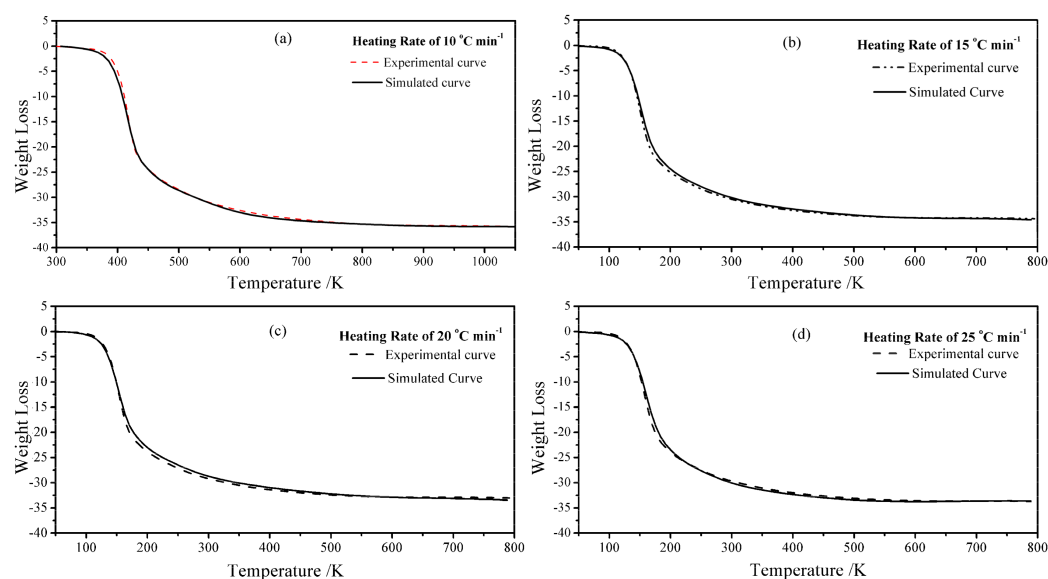


**Figure 6.** The comparison between the weight loss from experimental and simulated by deconvolution curves fitting method at four heating rates.

**The Mechanism Function Evaluation.** The  $g(\alpha)$  can be roughly observed by plotting of  $d\alpha/dT$  versus  $\alpha$  illustrated in Figure 7. The shapes of  $d\alpha/dT$  versus  $\alpha$  curve of the first and the second steps are the same as the shapes of the A or R models and the A or F models, respectively. The correct  $g(\alpha)$  models were evaluated by the master plots combined with the non-linear curve fitting (Equations (29)–(32)). Figure 8 illustrates the master plots fitted non-linear curves of the first and the second steps and the most probable mechanism functions are according to  $A_{1.25}$  for the first step and  $A_{1.61}$  for the second step. The most probable mechanism functions are according to  $A_{1.25}$  for the first step and  $A_{1.61}$  for the second step, that is the dehydrations of both steps are controlled by the random nucleation and consequent growth, A models with the different n-order. The correction of the mechanism functions fitted from the modified master plots method is double-checked using Equation (19). The  $g(\alpha)$  evaluated from the experiment is compared with the theoretical by minimizing the RSS (Equation (33)) and the results are shown in Figures 9 and 10. The results evaluated from Equation (19) agree well with the results fitting from the modified master plots method. The obtained results are shown more credible in the kinetics. Both function models obtained indicate a similar mechanism of sigmoid rate equations or random nucleation and subsequent growth. The models obtained in this work are different from one step as a single dehydration process with the F1/3 model controlling mechanism estimated by the Coats–Redfern method reported previously [7], which indicates that the different synthetic routes showed different thermal behavior and kinetic parameters [16,17].

**Table 1.** The calculated E, A, and % relative error of the three dehydration steps from the iterative modified KAS equation.

$\alpha$	Step I				Step II				Step III			
	E/kJ mol <sup>-1</sup>	%Error	R <sup>2</sup>	A/s <sup>-1</sup>	E/kJ mol <sup>-1</sup>	%Error	R <sup>2</sup>	A/s <sup>-1</sup>	E/kJ mol <sup>-1</sup>	%Error	R <sup>2</sup>	A/s <sup>-1</sup>
0.10	106.84	0.62	0.9947	$8.18 \times 10^{13}$	80.98	7.77	0.9819	$4.97 \times 10^{10}$	53.35	38.19	0.4372	-
0.12	105.88	0.49	0.9966	$5.25 \times 10^{13}$	81.07	8.75	0.9772	$4.16 \times 10^{10}$	51.90	38.55	0.4307	-
0.14	104.98	0.38	0.9980	$3.51 \times 10^{13}$	80.99	9.54	0.9730	$3.38 \times 10^{10}$	52.27	37.11	0.4570	-
0.16	104.32	0.28	0.9989	$2.56 \times 10^{13}$	80.84	10.21	0.9691	$2.73 \times 10^{10}$	51.71	37.29	0.4537	-
0.18	103.88	0.18	0.9996	$2.02 \times 10^{13}$	80.65	10.78	0.9655	$2.22 \times 10^{10}$	51.19	37.48	0.4502	-
0.20	103.08	0.09	0.9999	$1.44 \times 10^{13}$	80.45	11.26	0.9623	$1.81 \times 10^{10}$	51.08	36.80	0.4628	-
0.22	102.34	0.07	0.9999	$1.06 \times 10^{13}$	80.23	11.68	0.9593	$1.49 \times 10^{10}$	50.88	36.98	0.4595	-
0.24	101.72	0.13	0.9998	$8.11 \times 10^{12}$	80.01	12.05	0.9566	$1.23 \times 10^{10}$	50.68	37.18	0.4558	-
0.26	101.02	0.22	0.9993	$6.10 \times 10^{12}$	79.79	12.38	0.9541	$1.03 \times 10^{10}$	50.48	37.40	0.4517	-
0.28	100.40	0.29	0.9988	$4.72 \times 10^{12}$	79.57	12.67	0.9517	$8.62 \times 10^9$	50.17	37.13	0.4568	-
0.30	99.76	0.36	0.9982	$3.64 \times 10^{12}$	79.34	12.94	0.9495	$7.25 \times 10^9$	50.08	37.36	0.4524	-
0.32	99.02	0.43	0.9975	$2.74 \times 10^{12}$	79.12	13.19	0.9473	$6.13 \times 10^9$	49.98	37.62	0.4477	-
0.34	98.44	0.50	0.9965	$2.17 \times 10^{12}$	78.91	13.44	0.9452	$5.23 \times 10^9$	49.89	37.89	0.4427	-
0.36	97.79	0.56	0.9956	$1.68 \times 10^{12}$	78.69	13.65	0.9433	$4.47 \times 10^9$	49.61	37.94	0.4419	-
0.38	97.12	0.62	0.9946	$1.30 \times 10^{12}$	78.48	13.85	0.9414	$3.83 \times 10^9$	49.49	38.16	0.4377	-
0.40	96.47	0.68	0.9935	$1.02 \times 10^{12}$	78.25	14.03	0.9396	$3.27 \times 10^9$	49.37	38.41	0.4333	-
0.42	95.81	0.75	0.9923	$7.92 \times 10^{11}$	78.03	14.21	0.9378	$2.81 \times 10^9$	49.25	38.67	0.4286	-
0.44	95.14	0.80	0.9911	$6.16 \times 10^{11}$	77.80	14.38	0.9360	$2.41 \times 10^9$	49.14	38.94	0.4238	-
0.46	94.48	0.86	0.9899	$4.82 \times 10^{11}$	77.55	14.54	0.9343	$2.06 \times 10^9$	49.03	39.22	0.4187	-
0.48	93.82	0.91	0.9886	$3.78 \times 10^{11}$	77.30	14.69	0.9327	$1.76 \times 10^9$	48.92	39.51	0.4135	-
0.50	93.12	0.96	0.9872	$2.94 \times 10^{11}$	77.04	14.83	0.9310	$1.51 \times 10^9$	48.82	39.82	0.4081	-
0.52	92.43	1.02	0.9858	$2.28 \times 10^{11}$	76.77	14.97	0.9294	$1.28 \times 10^9$	48.72	40.14	0.4026	-

Table 1. Cont.

$\alpha$	Step I				Step II				Step III			
	E/kJ mol <sup>-1</sup>	%Error	R <sup>2</sup>	A/s <sup>-1</sup>	E/kJ mol <sup>-1</sup>	%Error	R <sup>2</sup>	A/s <sup>-1</sup>	E/kJ mol <sup>-1</sup>	%Error	R <sup>2</sup>	A/s <sup>-1</sup>
0.54	91.73	1.07	0.9844	$1.78 \times 10^{11}$	76.48	15.09	0.9277	$1.09 \times 10^9$	48.62	40.46	0.3969	-
0.56	91.02	1.12	0.9830	$1.38 \times 10^{11}$	76.18	15.22	0.9261	$9.19 \times 10^8$	48.53	40.80	0.3911	-
0.58	90.30	1.17	0.9815	$1.07 \times 10^{11}$	75.86	15.34	0.9244	$7.73 \times 10^8$	48.44	41.14	0.3852	-
0.60	89.57	1.21	0.9800	$8.24 \times 10^{10}$	75.51	15.43	0.9229	$6.46 \times 10^8$	48.35	41.50	0.3791	-
0.62	88.82	1.26	0.9784	$6.34 \times 10^{10}$	75.14	15.54	0.9212	$5.36 \times 10^8$	48.26	41.85	0.3731	-
0.64	88.05	1.30	0.9769	$4.86 \times 10^{10}$	74.74	15.63	0.9196	$4.41 \times 10^8$	48.17	42.24	0.3666	-
0.66	87.25	1.35	0.9753	$3.69 \times 10^{10}$	74.32	15.72	0.9179	$3.60 \times 10^8$	48.10	42.61	0.3605	-
0.68	86.41	1.39	0.9737	$2.77 \times 10^{10}$	73.87	15.79	0.9162	$2.92 \times 10^8$	48.02	43.01	0.3539	-
0.70	85.51	1.44	0.9721	$2.04 \times 10^{10}$	73.37	15.88	0.9143	$2.33 \times 10^8$	47.95	43.43	0.3471	-
0.72	84.53	1.48	0.9705	$1.47 \times 10^{10}$	72.82	15.96	0.9123	$1.83 \times 10^8$	47.90	43.83	0.3407	-
0.74	83.49	1.52	0.9688	$1.04 \times 10^{10}$	72.17	16.02	0.9103	$1.40 \times 10^8$	46.95	44.77	0.3257	-
0.76	82.37	1.56	0.9670	$7.21 \times 10^9$	71.54	16.05	0.9085	$1.07 \times 10^8$	45.30	46.35	0.3016	-
0.78	81.17	1.61	0.9653	$4.87 \times 10^9$	70.86	16.07	0.9067	$8.06 \times 10^7$	45.77	44.63	0.3280	-
0.80	79.89	1.65	0.9633	$3.22 \times 10^9$	70.09	16.10	0.9045	$5.91 \times 10^7$	47.41	44.90	0.3238	-
0.82	78.56	1.71	0.9611	$2.09 \times 10^9$	69.14	16.15	0.9016	$4.10 \times 10^7$	49.09	45.18	0.3194	-
0.84	77.21	1.77	0.9583	$1.35 \times 10^9$	68.13	16.17	0.8988	$2.80 \times 10^7$	50.81	45.48	0.3148	-
0.86	75.66	1.79	0.9573	$8.19 \times 10^8$	67.07	16.14	0.8962	$1.86 \times 10^7$	52.58	45.79	0.3101	-
0.88	74.05	1.83	0.9552	$4.88 \times 10^8$	65.87	16.10	0.8933	$1.19 \times 10^7$	54.38	46.12	0.3051	-
0.90	72.32	1.90	0.9521	$2.79 \times 10^8$	64.55	16.07	0.8897	$7.28 \times 10^6$	46.83	52.08	0.2233	-
average	91.86	1.31	0.9628	$5.98 \times 10^9$	75.85	16.06	0.816	$8.27 \times 10^7$	49.45	22.22	0.63	-

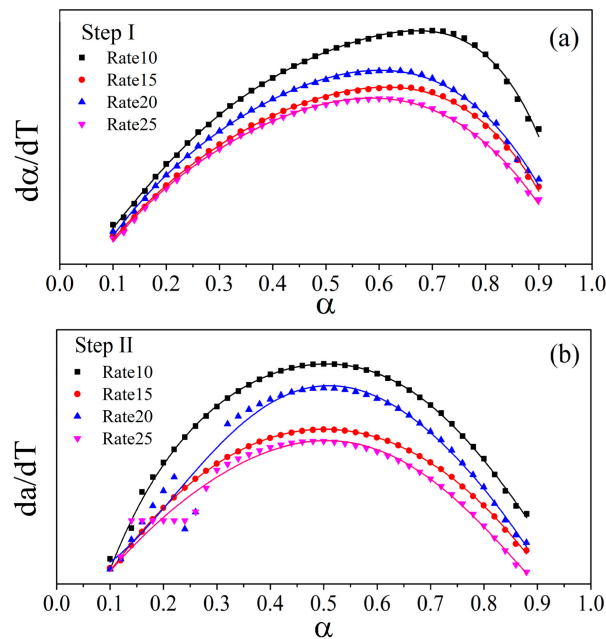


Figure 7. The  $d\alpha/dT$  versus  $\alpha$  curves of (a) the first and (b) the second steps.

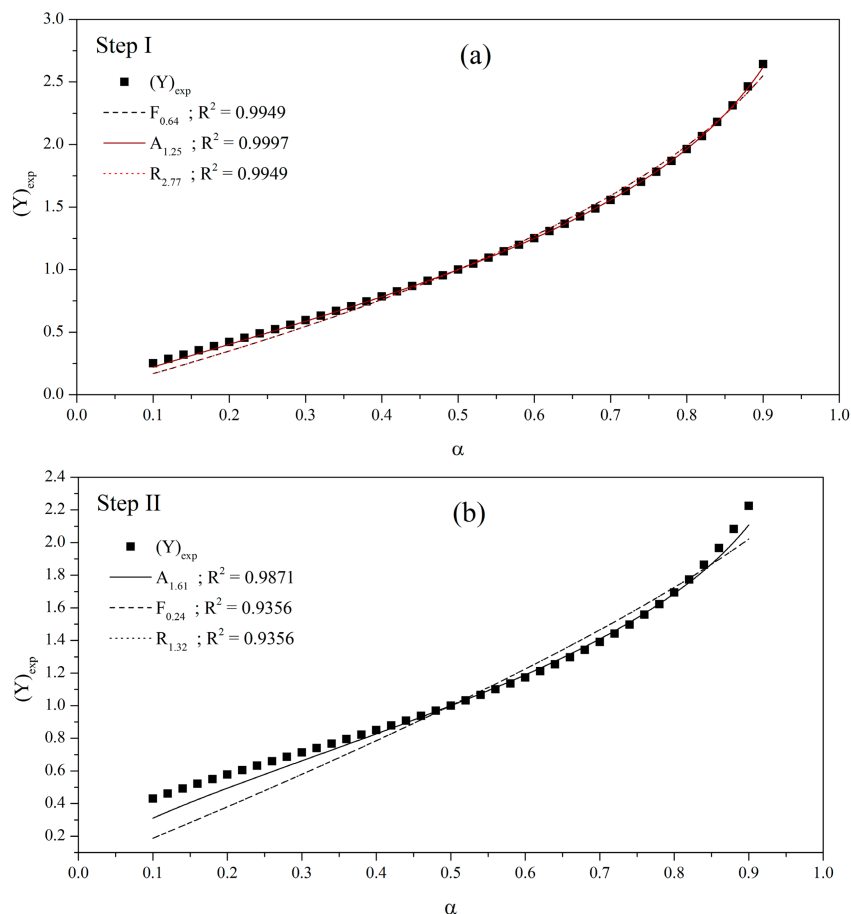
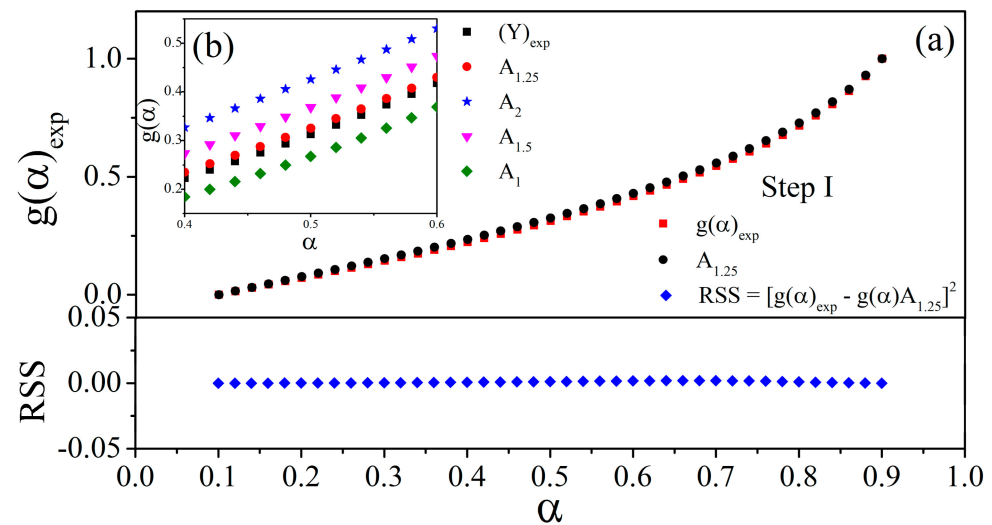
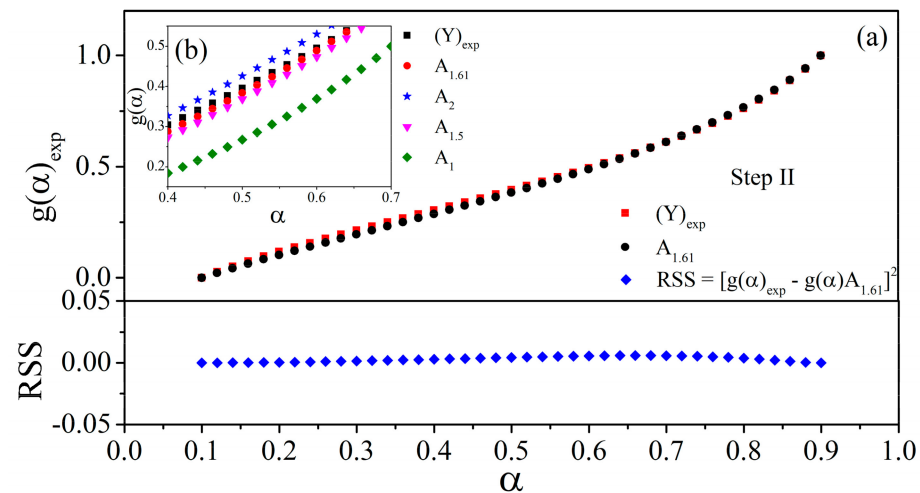


Figure 8. The fitted non-linear curves of (a) the first and (b) the second steps from the master plots combined with the non-linear curve fitting method. Comparative results between the experimental and model plots for (a) the first and (b) the second individual peaks obtained from  $Y(\alpha)$  plots of the studied thermal solid-state reaction.



**Figure 9.** The experimental and the theoretical plots (a,b) of the explored  $g(\alpha)$  versus  $\alpha$  curves using the reaction models for the first step.



**Figure 10.** The experimental and the theoretical plots (a,b) of the explored  $g(\alpha)$  versus  $\alpha$  curves using the reaction models for the second step.

#### 4. Conclusions

$\text{MgHPO}_4 \cdot 3\text{H}_2\text{O}$  was successfully synthesized by the simple precipitation for a short time (2 h) and thermally decomposed into a single dehydration process resulting from three overlapped steps in the range of 373–823 K. The final product showed thermal stability at above 773 K and the excellent crystallinity was recorded at about 921 K obtained from the complete exothermic DTA peak. The prepared sample and their final products obtained from heating at 773 and 973 K were analyzed by FTIR and XRD techniques. The temperature dependence of the standard  $\Delta S^\circ(T)$ ,  $\Delta H^\circ(T)$ , and  $\Delta G^\circ(T)$  determined using the cubic polynomial curve fitting was found that  $\Delta H^\circ(T)$  exhibits non-linear dependence of temperature, while  $\Delta S^\circ(T)$  and  $\Delta G^\circ(T)$  are logarithmic dependence of temperature, created from DSC data. The three steps of the dehydration process showed the overlapped peak in the DTG curve and the deconvolution technique using co-mathematical functions was used to separate individual peaks. The iterative modified KAS equation was used to calculate the E values independence on the conversion fraction with  $r^2$  (the correlation coefficient of linear regression) and the % relative error, which offer to discuss the physical meaning of kinetics. The first step shows the % relative errors are less than 10% indicating from the E dependent with the conversion fraction, while the second step is opposite and the third step is hard to explain on kinetics because of very low  $r^2$  values. Consequently, mechanisms

of the first, second, and third steps are the single dehydration process, the multi-step, and the parallel of the physical and chemical processes, respectively. The  $g(\alpha)$  models of the first and the second dehydration steps were determined by three methods (the roughly observed  $g(\alpha)$  by the plotting of  $d\alpha/dT$  versus  $\alpha$ , the exhaustive  $g(\alpha)$  evaluated using the modified master plots combined with the non-linear curve fitting and then the corrective  $g(\alpha)$  checked using the basic master plot equation), which obtained the results with good consistency. The random nucleation and consequent growth, A models with the different n-order, are the mechanism controlling the dehydration process of the first ( $A_{1.25}$ ) and the second ( $A_{1.61}$ ) steps. The results of the thermodynamics and kinetics of thermal decomposition of  $MgHPO_4 \cdot 3H_2O$  for the synthesized  $Mg_2P_2O_7$  are mandatory for researchers (academic scientists and industrialists) to refine the technology and make magnesium phosphate, which may be useful for potential applications as enamels, glazes, catalysts, etc.

**Supplementary Materials:** The following supporting information can be downloaded at: <https://www.mdpi.com/article/10.3390/cryst13040567/s1>, Table S1: Mathematical expressions for nucleation rates law [40]. Table S2. Algebraic expressions of kinetic functions and its corresponding mechanism [37]. Figure S1. One-dimensional diffusion through a flat plane [40]. Figure S2. Schematic representation of a spherical reaction [40].

**Author Contributions:** S.K.: investigation, experiment, data curation, writing—original draft, review and editing. S.T.: data curation, writing—review and editing. B.B.: conceptualization, investigation, writing—review and editing, supervision. P.R.: conceptualization, data curation, writing—review and editing. All authors have read and agreed to the published version of the manuscript.

**Funding:** King Mongkut’s Institute of Technology Ladkrabang, [KREF145907].

**Data Availability Statement:** All data that support the findings of this study are available from the corresponding author upon reasonable request.

**Acknowledgments:** We thank the Department of Chemistry, Faculty of Science, Khon Kaen University for providing research facilities. The financial support from the Advance Phosphate Material and Alternative Fuel Energy Research Unit, Department of Chemistry, Faculty of Science, King Mongkut’s Institute of Technology Ladkrabang, [KREF145907], is gratefully acknowledged. The authors would like to thanks the Scientific Instruments Center KMITL for supporting TGA, FTIR, XRD, and SEM techniques.

**Conflicts of Interest:** The authors declare no conflict of interest.

## References

- Muryanto, S. On precipitation of struvite ( $MgNH_4PO_4 \cdot 6H_2O$ ). *J. Sci. Sci. Educ.* **2017**, *1*, 21–29. [[CrossRef](#)]
- Mesíková, Ž.; Šulcová, P.; Trojan, M. Synthesis and characterization of newberyite. *J. Therm. Anal. Calorim.* **2007**, *88*, 103–106. [[CrossRef](#)]
- Takagi, S.; Mathew, M.; Brown, W.E. Crystal structures of bobierrite and synthetic  $Mg_3(PO_4)_2 \cdot 8H_2O$ . *Am. Mineral.* **1986**, *71*, 1229–1233.
- Frost, R.L.; Weier, M.L.; Martens, W.N.; Henry, D.A.; Mills, S.J. Raman spectroscopy of newberyite, hannayite and struvite. *Spectrochim. Acta A* **2005**, *62*, 181–188. [[CrossRef](#)]
- Tamimi, F.; Nihouannen, D.L.; Bassett, D.C.; Ibasco, S.; Gbureck, U.; Knowles, J.; Wright, A.; Flynn, A.; Komarova, S.V.; Barralet, J.E. Biocompatibility of magnesium phosphate minerals and their stability under physiological conditions. *Acta Biomater.* **2011**, *7*, 2678–2685. [[CrossRef](#)] [[PubMed](#)]
- Kurtulus, G.; Tas, A.C. Transformations of neat and heated struvite ( $MgNH_4PO_4 \cdot 6H_2O$ ). *Mater. Lett.* **2011**, *65*, 2883–2886. [[CrossRef](#)]
- Boonchom, B. Kinetic and thermodynamic studies of  $MgHPO_4 \cdot 3H_2O$  by non-isothermal decomposition data. *J. Therm. Anal. Calorim.* **2009**, *98*, 863–871. [[CrossRef](#)]
- Bayuseno, A.P.; Perwitasari, D.S.; Muryanto, S.; Tauviquirrahman, M.; Jamari, J. Kinetics and morphological characteristics of struvite ( $MgNH_4PO_4 \cdot 6H_2O$ ) under the influence of maleic acid. *Heliyon* **2020**, *6*, e03533. [[CrossRef](#)]
- Bhuiyan, M.I.H.; Mavinic, D.S.; Koch, F.A. Thermal decomposition of struvite and its phase transition. *Chemosphere* **2008**, *70*, 1347–1356. [[CrossRef](#)]
- Boonchom, B. Kinetics of thermal transformation of  $Mg_3(PO_4)_2 \cdot 8H_2O$  to  $Mg_3(PO_4)_2$ . *Int. J. Thermophys.* **2010**, *31*, 416–429. [[CrossRef](#)]

11. Şenberber, F.T.; Derun, E.M. Thermal kinetics and thermodynamics of the dehydration reaction of  $\text{Mg}_3(\text{PO}_4)_2 \cdot 22\text{H}_2\text{O}$ . *Eurasian J. Biol. Chem. Sci.* **2019**, *2*, 47–51.
12. Marcu, I.-C.; Sandulescu, I.; Millet, J.-M.M. Oxidationhydrogenation of *n*-butane over tetravalent metal phosphates based catalysts. *Appl. Catal. A Gen.* **2002**, *227*, 309–320. [[CrossRef](#)]
13. Aramendia, M.A.; Borau, V.; Jiménez, C.; Marinas, J.M.; Romero, F.J. Synthesis and characterization of magnesium phosphates and their catalytic properties in the conversion of 2-hexanol. *J. Colloid Interface Sci.* **1999**, *217*, 288–298. [[CrossRef](#)]
14. Sadiq, M.; Abdennouri, M.; Barka, N.; Baâlala, M.; Lamonier, C.; Bensitel, M. Influence of the crystal phase of magnesium phosphates catalysts on the skeletal isomerization of 3,3-dimethylbut-1-ene. *Can. Chem. Trans.* **2015**, *3*, 225–233.
15. Llusar, M.; Zielinska, A.; Tena, M.A.; Badenes, J.A.; Monrós, G. Blue-violet ceramic pigments based on Co and Mg  $\text{Co}_{2-x}\text{Mg}_x\text{P}_2\text{O}_7$  diphosphates. *J. Eur. Ceram. Soc.* **2010**, *30*, 1887–1896. [[CrossRef](#)]
16. Ostrowski, N.; Roy, A.; Kumta, P.N. Magnesium phosphate cement systems for hard tissue applications: A review. *ACS Biomater. Sci. Eng.* **2016**, *2*, 1067–1083. [[CrossRef](#)] [[PubMed](#)]
17. Chong, L.; Shi, C.; Yang, J.; Jia, H. Effect of limestone powder on the water stability of magnesium phosphate cement-based materials. *Constr. Build. Mater.* **2017**, *148*, 590–598. [[CrossRef](#)]
18. Aramendia, M.A.; Borau, V.; Jiménez, C.; Marinas, J.M.; Romero, F.J.; Ruiz, J.R. Characterization by XRD, DRIFT, and MAS NMR spectroscopies of a  $\text{Mg}_2\text{P}_2\text{O}_7$  catalyst. *J. Colloid Interface Sci.* **1998**, *202*, 456–461. [[CrossRef](#)]
19. Sadiq, M.; Sahibed-dine, A.; Baalala, M.; Nohair, K.; Abdennouri, M.; Bensitel, M.; Lamonier, C.; Leglise, J. Influence of acid–base properties of cobalt–molybdenum catalysts supported on magnesium orthophosphates in isomerization of 3,3-dimethylbut-1-ene. *Arab. J. Chem.* **2011**, *4*, 449–457. [[CrossRef](#)]
20. Sugiyama, S.; Yokoyama, M.; Ishizuka, H.; Sotowa, K.-I.; Tomida, T.; Shigemoto, N. Removal of aqueous ammonium with magnesium phosphates obtained from the ammonium-elimination of magnesium ammonium phosphate. *J. Colloid Interface Sci.* **2005**, *292*, 133–138. [[CrossRef](#)]
21. Mohammad, F.; Arfin, T.; Al-Lohedan, H.A. Sustained drug release and electrochemical performance of ethyl cellulose-magnesium hydrogen phosphate composite. *Mater. Sci. Eng. C* **2017**, *71*, 735–743. [[CrossRef](#)]
22. Kissinger, H.E. Reaction kinetics in differential thermal analysis. *Anal. Chem.* **1957**, *29*, 1702–1706. [[CrossRef](#)]
23. Akahira, T.; Sunose, T. Method of determining activation deterioration constant of electrical insulating materials. *Res. Rep. Chiba Inst. Technol.* **1971**, *16*, 22–31.
24. Kullyakool, S.; Siritwong, K.; Noisong, P.; Danvirutai, C. Kinetic triplet evaluation of a complicated dehydration of  $\text{Co}_3(\text{PO}_4)_2 \cdot 8\text{H}_2\text{O}$  using the deconvolution and the simplified master plots combined with nonlinear regression. *J. Therm. Anal. Calorim.* **2017**, *127*, 1963–1974. [[CrossRef](#)]
25. Perejón, A.; Sánchez-Jiménez, P.E.; Criado, J.M.; Pérez-Maqueda, L.A. Kinetic analysis of complex solid-state reactions. A new deconvolution procedure. *J. Phys. Chem. B* **2011**, *115*, 1780–1791. [[CrossRef](#)]
26. Zhang, S.; Zhang, J.; Kou, K.; Jia, Q.; Xu, Y.; Liu, N.; Hu, R. Standard enthalpy of formation, thermal behavior, and specific heat capacity of 2HNIW·HMx co-crystals. *J. Chem. Eng. Data* **2019**, *64*, 42–50. [[CrossRef](#)]
27. Chirico, R.D.; Steele, W.V. Thermodynamic properties of 2-methylquinoline and 8-methylquinoline. *J. Chem. Eng. Data* **2005**, *50*, 697–708. [[CrossRef](#)]
28. Perwitasari, D.S.; Muryanto, S.; Schmahl, W.W.; Jamari, J.; Bayuseno, A.P. A kinetic and structural analysis of the effects of Ca- and Fe ions on struvite crystal growth. *Solid State Sci.* **2022**, *134*, 107062. [[CrossRef](#)]
29. Viani, A.; Zárýbnická, L.; Ševčík, R.; Mácová, P.; Machotová, J.; Veltruská, K. Struvite-K crystal growth inhibition by citric acid: Formation of complexes in solution and surface adsorption effects. *J. Cryst. Growth* **2022**, *598*, 126858. [[CrossRef](#)]
30. Ambekar, A.; Yoh, J.J. Chemical kinetics of multi-component pyrotechnics and mechanistic deconvolution of variable activation energy. *Proc. Combust. Inst.* **2019**, *37*, 3193–3201. [[CrossRef](#)]
31. Kullyakool, S.; Boonchom, B.; Chaiseeda, K. Simple synthesis, kinetics and thermodynamics of rod-like  $\text{Cu}_2(\text{OH})\text{PO}_4$  microparticles and rod-like  $\text{Cu}_4\text{O}(\text{PO}_4)_2$  nanoparticles. *Mater. Chem. Physics* **2020**, *250*, 123158. [[CrossRef](#)]
32. Chaudhary, R.G.; Ali, P.; Gandhare, N.V.; Tanna, J.A.; Juneja, H.D. Thermal decomposition kinetics of some transition metal coordination polymers of fumaroyl bis (paramethoxyphenylcarbamide) using DTG/DTA techniques. *Arabian J. Chem.* **2019**, *12*, 1070–1082. [[CrossRef](#)]
33. Devi, P.; Singh, K.; Kubavat, B. Synthesis, spectroscopic, quantum, thermal and kinetics, antibacterial and antifungal studies: Novel Schiff base 5-methyl-3-((5-bromosalicylidene) amino)- pyrazole and its transition metal complexes. *Res. Chem.* **2023**, *5*, 100813. [[CrossRef](#)]
34. Kullyakool, S.; Siritwong, K.; Noisong, P.; Danvirutai, C. Studies of thermal decomposition kinetics and temperature dependence of thermodynamic functions of the new precursor  $\text{LiNiPO}_4 \cdot 3\text{H}_2\text{O}$  for the synthesis of olivine  $\text{LiNiPO}_4$ . *J. Therm. Anal. Calorim.* **2015**, *122*, 665–677. [[CrossRef](#)]
35. Cheng, Z.; Wu, W.; Ji, P.; Zhou, X.; Liu, R.; Cai, J. Applicability of Fraser–Suzuki function in kinetic analysis of DAEM processes and lignocellulosic biomass pyrolysis processes. *J. Therm. Anal. Calorim.* **2015**, *119*, 1429–1438. [[CrossRef](#)]
36. Senum, G.I.; Yang, R.T. Rational approximations of the integral of the Arrhenius function. *J. Therm. Anal.* **1977**, *11*, 445–447. [[CrossRef](#)]
37. Vyazovkin, S.; Burnham, A.K.; Criado, J.M.; Pérez-Maqueda, L.A.; Popescu, C.; Sbirrazzuoli, N. ICTAC Kinetics Committee recommendations for performing kinetic computations on thermal analysis data. *Thermochim. Acta* **2011**, *520*, 1–19. [[CrossRef](#)]

38. Galwey, A.K. Is the science of thermal analysis kinetics based on solid foundations? A literature appraisal. *Thermochim. Acta* **2004**, *413*, 139–183. [[CrossRef](#)]
39. Gotor, F.J.; Criado, J.M.; Malek, J.; Koga, N. Kinetic analysis of solid-state reactions: the universality of master plots for analyzing isothermal and nonisothermal experiments. *J. Phys. Chem. A* **2000**, *104*, 10777–10782. [[CrossRef](#)]
40. Khanwan, A.; Flanagan, D.R. Solid-state kinetic models: Basics and mathematical fundamentals. *J. Phys. Chem.* **2006**, *110*, 17315–17328.

**Disclaimer/Publisher’s Note:** The statements, opinions and data contained in all publications are solely those of the individual author(s) and contributor(s) and not of MDPI and/or the editor(s). MDPI and/or the editor(s) disclaim responsibility for any injury to people or property resulting from any ideas, methods, instructions or products referred to in the content.